Optical Coherence Tomography Imaging by a Fully Integrated MOEMS Endomicroscopy Probe With Mirau Microinterferometer and Two-Axis Electrothermal Microscanner Using Lissajous Trajectory Scanning

Przemysław Struk, Sylwester Bargiel, Michal Józwik, Bartosz Mirecki, Maciej Wojtkowski, Huikai Xie, *Fellow, IEEE*, and Christophe Gorecki

***Abstract*—This article presents the results of a study focused on the development of an integrated probe intended for endomicroscopic application. A new type of transverse scanning probe is described, which was built using Mirau microinterferometer fabricated in micro-opto-electromechanical systems (MOEMS) technology, and a two-axis electrothermal actuator fabricated in micro-electromechanical systems (MEMS) technology, connected with a gradient-index (GRIN) lens collimator and single-mode fiber. Herein, we present a numerical analysis and an optimization of endomicroscopic probe-scanning properties, based on Lissajous curves. The key part of this article is 2-D and 3-D imaging of phantom structures, based on polymer material, light-scattering material, and USAF-target pattern visualized with an endomicroscopy probe. The imaging was obtained by the swept source optical coherence tomography (SS-OCT) technique, working at a central wavelength $\lambda_c = 1060$ nm, a swept range $\Delta\lambda = 100$ nm, an A-scan rate $f_a = 200$ kHz, and the scanning of samples with the use of Lissajous curves.**

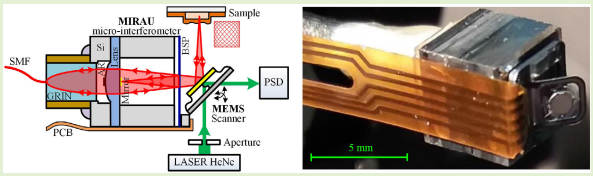

***Index Terms*— Endomicroscopy probe, Lissajous scanning, micro-electromechanical systems (MEMS) two-axis electrothermal actuator, micro-opto-electromechanical systems (MOEMS) Mirau microinterferometer, optical coherence tomography (OCT).**

I. Introduction

A KEY issue of modern technique is the development of noninvasive, fast, accurate, and reliable diagnostic methods for imaging the sample into hard-to-reach places such as holes and cavities [1], [2], [3]. One of the most attractive method for 2-D and 3-D imaging investigated structure in hard-to-reach places is the optical coherence tomography (OCT) technique combined with endomicroscopic device [4], [5], [6], [7], [8]. The OCT method offers 3-D optical imaging with high resolution at the level of a few micrometers and a fast scanning rate at the level of several hundred kHz [8], [9], [10].

An especially challenging aspect of 2-D and 3-D optical imagining of the investigated structure has been the development of miniaturized tools, in the form of endomicroscopy probes [11], [12], [13], [14]. Micro-opto-electromechanical systems and micro-electromechanical systems (MOEMS/MEMS) technology is particularly suitable for large-scale production of miniaturized micro-optical and micromechanical components that can be integrated, and thus used to develop endomicroscopic probes [14], [15], [16], [17]. One of the most important issues in endomicroscopy probes using the OCT technique is the selection of the proper method of scanning the sample. The choice of the scanning method is dictated by the construction of the probe or the type of actuator used to move the mirror, which causes a change in the position of the scanning beam on the sample being examined.

Manuscript received 4 January 2024; revised 21 February 2024; accepted 28 February 2024. Date of publication 18 March 2024; date of current version 1 May 2024. This work was supported in part by the Labex Action Program under Grant ANR-11-LABX-0001-01, in part by the Project “Robotics and Optical Coherence Tomography (OCT) for BiOpsy in the Digestive Tract” (ROBOT) under Grant INSERM Robot 2017-0123, in part by the French National Nanofabrication Network (RENATECH) and Its Franche-Comté Electronics Mechanics Thermal Science and Optics – Sciences and Technologies (FEMTO-ST) Technological Facility, in part by the Collegium French-Swiss scientific alliance cross the borders of science, Smart Systems for a better life (SMYLE), in part by the Silesian University of Technology Rector’s Pro-Quality under Grant 05/040/RGJ20/2003, and in part by the National Science Center under Grant 2020/38/L/ST2/00556. The associate editor coordinating the review of this article and approving it for publication was Prof. Jeong Bong Lee. *(Corresponding author: Przemysław Struk.)*

Please see the Acknowledgment section of this paper for the author affiliations.

Digital Object Identifier 10.1109/JSEN.2024.3373223

Among the available endomicroscopic probes, the following sample-scanning solutions can be applied: probe rotation, microprism rotation, and micromirror movement [14], [15], [16], [17], [18]. Especially, remarkable is scanning by MEMS micromirror, which can be controlled by raster scanning, circular scanning, and Lissajous scanning [9], [10], [11], [12], [13], [14], [15], [16], [17], [18], [19], [20], [21], [22]. The application of the scanning trajectory using Lissajous curves is an effective method for controlling the MEMS two-axis electrothermal actuators with the micromirror. This technique enables smooth changes in the direction of movement for the scanning mirror in electrothermal MEMS actuators. Furthermore, the frequencies and amplitudes of mirror movement on the x- and y-axes can be precisely controlled, which enables the attainment of a high density of trajectory and thus precise scanning and finally high-quality OCT imaging of the sample being examined [23], [24], [25], [26], [27]. This article presents an innovative, fully integrated MOEMS endomicroscopy probe that simultaneously combines beam-forming optics, an interferometric system, and a scanning device using Lissajous patterns to scan the sample. The device is a Mirau microinterferometer integrated with a two-axis electrothermal actuator with a scanning mirror and connected with a gradient-index (GRIN) lens collimator. The advantages of this solution are the small size of the probe, the production of probe components at the wafer level (229 structures on a 4-in wafer), and the high scale of integration in MOEMS technology [17]. The probe is resistant to external conditions, and there is no necessary compensation for the difference in optical paths in the interferometer arms as in the case of probes with an external Michelson interferometer.

The endomicroscopic probes presented so far using MEMS actuators with mirrors do not contain an interferometric circuit integrated in the probe. These are generally systems in the configuration of a Michelson interferometer, which is located outside the endomicroscopic probe [14], [15], [16], [18], [19], [20]. In this type of system, probes usually include a light beam forming optics, most often a GRIN lens or microlens and a MEMS mirror scanner [14], [16], [18], [19], [20].

The first part of this article focuses on the numerical analysis aimed at optimizing the scanning of the structures of the samples. Then, we present the experimental results of the OCT imaging, using an endomicroscopic probe that we developed. We used the Lissajous trajectory to scan selected samples, such as the USAF 1951 target, a phantom in the form of a thin ~20-mm pattern based on a polymer material (photoresist S1813) deposited on a glass substrate, and a phantom with light-scattering properties in the form of a scotch tape on a glass substrate.

In the future, the presented probe will have potential applications, among others, in endoscopic devices for scanning and lesion detection in the upper human digestive tract.

II. Measurement Setup

The key component of the OCT setup is an endomicroscopy probe, which consists of a GRIN lens collimator (size: 20 mm length and 1.9-mm outer diameter) (GRINTech, Jena, Germany), Mirau microinterferometer (size: 5.3 × 4.8 × 4.8 mm), and a two-axis electrothermal microscanner (size:

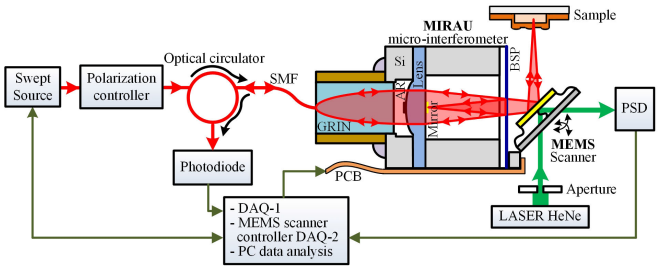

Fig. 1. Schematic of the measurement setup and endomicroscopy probe (SMF—single-mode fiber, BSP—beam splitter plate, PSD—position sensing detector, and AR—antireflection coating).

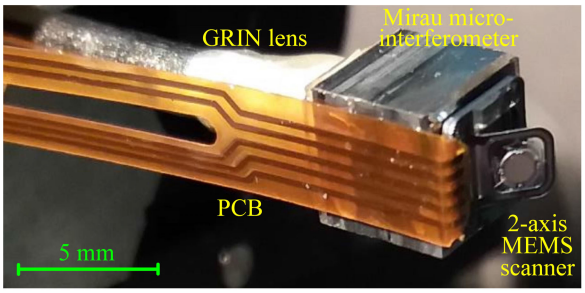

Fig. 2. Photograph of the endomicroscopic probe.

0.5 mm thickness of scanner substrate and 2.2 mm height of frame with scanning mirror). The final size of the packaged probe is 28.0 × 4.8 mm (length × width at its widest point).

The schematic of the measurement setup as well as a photograph of the endomicroscopy probe are presented in Figs. 1 and 2, respectively. It should be mentioned that the endomicroscopy probe can work in two modes of scanning: the forward scanning mode, which was presented in [17] and [28], and the transverse scanning mode, introduced for the first time in this article. The forward scanning mode described in [17] and [28] is intended for scanning in easily accessible locations, where the probe can be placed directly in front of the scanned structure. For harder-to-reach places where forward scanning is not possible, a transverse scanning probe is provided. The transverse scanning mode uses a fully integrated probe with a Mirau microinterferometer, linked to a two-axis electrothermal scanner placed on it. The scanning beam focused by a lens in the Mirau microinterferometer is reflected by a 1-mm-diameter micromirror, suspended on four electrothermal actuators in the scanner frame. Changing the tilt of the mirror in the scanner changes the position of the scanning beam in accordance with the Lissajous trajectory. A detailed description of the fabrication technology of the Mirau microinterferometer, as well as the two-axis electrothermal scanner, has been presented previously [17], [27].

The experimental measurement setup consists of the following components: a light source—swept source with central wavelength $\lambda_c = 1060$ nm, swept range $\Delta\lambda = 100$ nm, A-scan rate $f_a = 200$ kHz, and output power $P = 15$ mW (Axsun, Billerica, MA, USA, 1060 nm); a polarization controller (Thorlabs, Newton, NJ, USA, FCP024); an optical circulator (Fibrain, Zaczernie, Poland, 1060); and a single-mode fiber (SMF) circuit. The interferometric signal from the Mirau microinterferometer is directed by an optical circulator to a single point detector—photodiode (Wieserlabs, Penzberg, Germany, WL-BPD1GA), and the signal is measured with

a data acquisition card DAQ_1 (Alazartech, Pointe-Claire, Canada, ATS9373). The position of the scanning mirror, and thus the position of the scanning beam, is determined by the position sensing detector (PSD) (Thorlabs, PDP90A). The second side of the scanning mirror in the electrothermal actuator is illuminated by a He–Ne laser $\lambda = 632.8$ nm, with optical power $P = 5$ mW (Thorlabs). The aperture $d_A = 1$ mm is used to match the diameter of the laser beam to the diameter of the mirror in the scanner. The light beam reflected by the scanning mirror illuminates the PSD; next, the signal from the PSD is measured by a PSD control unit (Thorlabs, KPA101—K-Cube). The signal from the PSD control unit in the form of x and y coordinates (voltage signal) is acquired by a DAQ_2 data acquisition card (National Instrument, Austin, TX, USA, NI6363). The localization of the focused light beam is sampled at $f_s = 200$ kHz, and it is synchronized with the acquisition of OCT A-scans via a trigger output from the swept source. The scanning mirror is moved by four electrothermal actuators (two actuators per axis, placed on opposite edges of the scanning mirror) stimulated by four sinusoidal signals; i.e., one signal for each actuator to obtain the Lissajous trajectory. The x-axis is controlled by two sinusoidal signals of the same amplitude and frequency f_x, but the phase is shifted by 180°. The y-axis is controlled in the same way by two sinusoidal signals with the same frequency f_y and amplitude, but the phase is shifted by 180°. The phase shift of 180° between the control signals on a given axis causes each actuator to move simultaneously in the opposite direction, which results in the tilt of the mirror, which is suspended on the actuators from the equilibrium position. The dc voltage signal $U_{dc} = 2$ V is applied for setting the mirror in the correct position relative to the scanning light beam (in the optical axis) incoming from Mirau microinterferometer. The ac sinusoidal signal $U_{ac} = 0.06$ V is used for moving the scanning mirror. The selection of voltage has been selected for safety operation conditions for the electrothermal actuator both electrical (risk of burnout) and mechanical properties. Too large U_{ac} voltage amplitude and thus the deflection amplitude may cause mechanical coupling between the axes and disruption of the Lissajous trajectory.

The electric signals are delivered to the MEMS scanner by a flexible printed circuit board (PCB). The sine signals are generated by the DAQ_2 (National instrument, NI 6363) and amplified by an external operational amplifier (LM358P, Texas Instruments, Dallas, TX, US) with a gain equal to $G = 1$ to provide a sufficient current capacity at the level of $I_a = 20$ mA, which is used by the MEMS scanner. The amplifier contains voltage protection based on the Zener diode (1N4731A, Vishay Semiconductors, Shelton, CT, USA) against unwanted voltage spikes that could damage the actuators.

The scanning positions measured by PSD are used to verify the trajectory of the second beam (marked green in Fig. 1) reflected by the back part of the mirror at the MEMS scanner. The distances from the MEMS mirror to the PSD or the sample are different. Distance from the MEMS mirror to the sample is short and directly results from the Mirau design of the interferometer. Thus, to achieve the best result, the measured sample has to be placed in the focus of the probe.

The axial resolution of the probe depends on the parameters of the applied swept source, and it is determined by the following equation [29], [30]:

$$A_R = \frac{2 \cdot \ln(2) \cdot \lambda_c^2}{\pi \cdot \Delta\lambda} = 4.96\mu\text{m} \quad (1)$$

where $\lambda_c = 1060$ nm, central wavelength, and $\Delta\lambda = 100$ nm, the tuning range of the swept source.

The lateral resolution depends on the optical circuit used in the endomicroscopic probe, and it is defined by the following equation [29], [30]:

$$L_R = \frac{4 \cdot \lambda_c \cdot f_M}{\pi \cdot D} = 12.15\mu\text{m} \quad (2)$$

where λ_c = central wavelength; $f_M = 9$ mm, focal length; and $D = 1$ mm, the spot size of the light beam that illuminates the focusing lens in the Mirau microinterferometer.

During the numerical analysis and presentation of the experimental results, we used an Airy disk distribution of the light beam at the focus (first-order Bessel function). The diameter of the Airy disk can be calculated based on the following equation [31]:

$$d_{Airy} = \frac{2.44 \cdot \lambda_c \cdot f_M}{D} = 23.27\mu m. \quad (3)$$

Reliable OCT imaging reconstruction requires optimized spatial sampling matched to the size of the focused beam. The pixel size can be calculated based on the Nyquist–Shannon sampling theory, according to which the pixel size should be less than the full-width at half-maximum (FWHM)/2 of the point spread function (Airy disk). However, oversampling with FWHM/3 can be used to achieve better imaging quality, according to the following equation [27], [32], [33]:

$$\text{Pixel size} = \frac{\text{FWHM}}{3} = \frac{9.82\mu\text{m}}{3} = 3.27\mu\text{m} \quad (4)$$

where FWHM = 9.82 μm, half-width at half-maximum of the Airy disk (the first order of Bessel function).

III. Selection of Scanning Parameters

An important part of this study was the determination of the frequency characteristics of the electrothermal actuator with a scanning micromirror, which was attached to a Mirau microinterferometer. The frequency characteristics are essential for determining the proper operating parameters of the OCT probe when scanning the sample. The selection of the operating frequency of an electrothermal actuator is a compromise between obtaining the largest possible scanning area (maximum amplitude of mirror deflection in the x- and y-axes) and avoiding actuator operation near the resonant frequency, for which there is strong mechanical coupling between the x- and y-axes of the actuator. The frequency characteristics of the electrothermal actuator used in the current probe are shown in Fig. 3. The mirror deflection amplitude on the x- and y-axes was normalized to the unit value "1," taking account of the maximum amplitude on the x-axis as a reference, and thus, the relation of amplitude deflection scale on both axes was preserved. In addition, the actuator-operating frequency should be selected so that the amplitude difference between

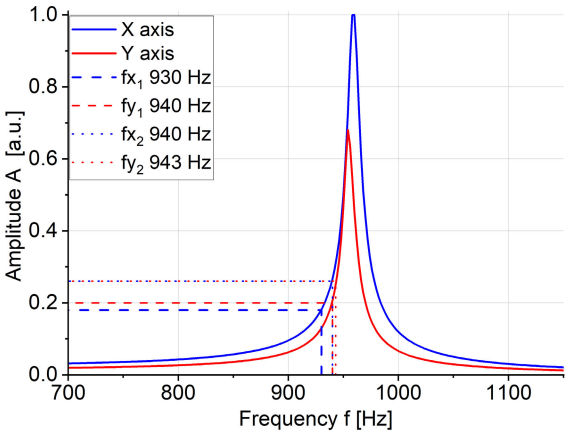

Fig. 3. Frequency characteristics of the MEMS electrothermal actuator mounted on the Mirau microinterferometer, with marked operating points.

the x- and y-axes is as small as possible to ensure a similar field of view on the x- and y-axes. Taking into account the above factors, two pairs of operating frequencies of the electrothermal actuator were selected for scanning the sample using the Lissajous trajectory

$f_{x1} = 930$ Hz; $f_{y1} = 940$ Hz (dashed line);

$f_{x2} = 940$ Hz; $f_{y2} = 943$ Hz (dotted line).

For the first pair of frequencies (f_{x1}, f_{y1}), the amplitudes of the scanning mirror's deflection are slightly different from each other, resulting in slightly different scanning ranges on the x- and y-axes. For the second frequency pair (f_{x2}, f_{y2}), the amplitude of the scanning mirror deflection is the same, so the scanning ranges on the x- and y-axes are virtually the same. The scanning area of the endomicroscopic probe for the aforementioned frequencies is discussed and evaluated experimentally in Section VI, and summarized in Table Table I.

IV. Numerical Analysis of Scanning Properties of Endomicroscopy Probe

A. Numerical Analysis of Light Beam Displacement During Scanning on the z-Axis

The purpose of the numerical analysis was to determine the possible curvature of the OCT image of the scanned surface, resulting from the use of a scanning mirror in an electrothermal actuator. The analysis was performed for a scan area on the x- and y-axes equal to $S_{A1} = 71.47 \times 86.48$ μm (corresponding to two operating frequencies $f_{x1} = 930$ Hz and $f_{y1} = 940$ Hz) or $S_{A2} = 110.58 \times 110.05$ μm (corresponding to two operating frequencies $f_{x1} = 930$ Hz and $f_{y1} = 940$ Hz). The scan areas were calculated based on the analysis of USAF 1951 target 2-D OCT images; a detailed description is provided in Section VI and Table I.

The numerically calculated sagitta of the scanning beam trajectory on the z-axis in the scanning area is $Sag_1 = 0.35$ μm for the scan field S_{A1} [Fig. 4(a)] and $Sag_2 = 0.67$ μm for the scan field S_{A2} [Fig. 4(b)]. The radius of curvature along which the scanning beam moves is 9 mm, which corresponds to the focal length of the glass lens in the Mirau microinterferometer. The analysis showed that the sagitta value of the scanning beam trajectory in the scanning area is several times smaller than the axial resolution of the endomicroscopy probe, which is $A_r = 4.96$ μm. In addition, the theoretically determined depth of focus of the lens applied in the Mirau microinterferometer is DOF = 218.64 μm, and it is much bigger than the calculated sagitta of the scanning beam trajectory. On this basis, it can be concluded that the curvature resulting from the use of scanning the sample with a mirror placed in an electrothermal actuator does not affect the OCT images that are obtained.

TABLE I
Scanning Properties of the Probe

Scanning area 1 (S_{A1})		Scanning area 2 (S_{A2})	
x-axis	y-axis	x-axis	y-axis
Frequency, Hz			
f_{x1}	f_{y1}	f_{x2}	f_{y2}
930	940	940	943
Scanned area, µm			
71.47	86.48	110.58	110.05
Accuracy of the scanning area field, µm			
$\Delta(S_{A1})$		$\Delta(S_{A2})$	
+/- 0.37		+/- 0.57	
Image resolution, pixels			
22	27	34	34

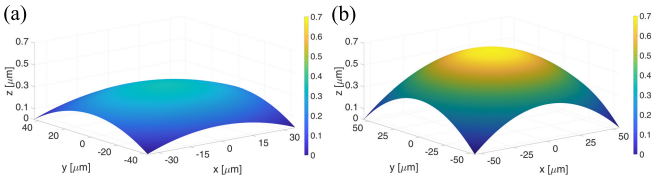

Fig. 4. Analysis of surface curvature on the z-axis of the scanning area: (a) $S_{A1} = 71.47 \times 86.48$ μm and (b) $S_{A2} = 110.58 \times 110.05$ μm.

B. Analysis of Field of View and Scan Density

Due to the harmonic nature of mirror motion, the work of the two-axis electrothermal scanner can be defined by Lissajous patterns. Lissajous curves are the path of a parametric point, defined by the superimposition of two perpendicular harmonic movements. Their shape depends on the amplitude, frequency ratio, and phase shift. In a 2-D space, the position of each point at a given time t is defined by x and y coordinates. It can be determined by the following formulas:

$$x(t) = A \cdot \sin(2\pi \cdot f_1 \cdot t + \delta)$$
$$y(t) = B \cdot \sin(2\pi \cdot f_2 \cdot t) \quad (5)$$

where A and B correspond to the x- and y-axes amplitudes, respectively; f_1 and f_2 represent the frequencies of the x- and y-axes, respectively; and δ corresponds to the initial phase shift.

If the ratio of the frequencies of the orthogonal harmonic motions is a rational number, then the figure related to movement is closed. This means that some areas of the test sample will not be scanned. The solution to this primary problem is

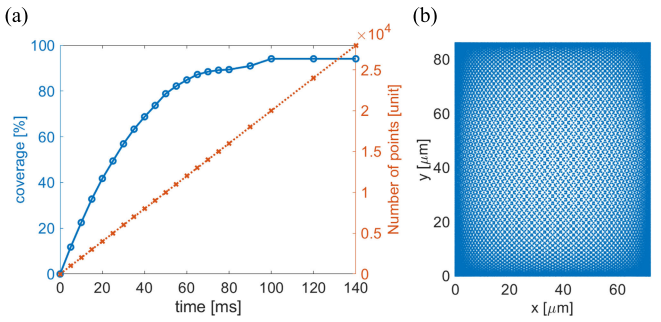

Fig. 5. Numerical data analysis of S_{A1} for $f_{x1} = 930$ Hz and $f_{y1} = 940$ Hz. (a) Graph of percent coverage of the measurement field versus time. (b) 2-D points distribution after $t = 100$ ms; 20 000 points; and coverage = 94.11%.

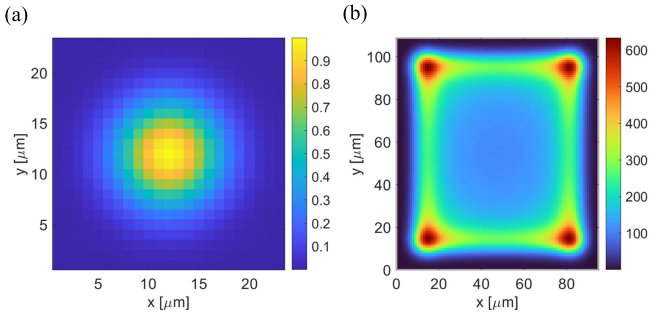

Fig. 6. (a) Airy spot on the 23 × 23 μm area for a single measurement point. (b) Intensity distribution for the entire field S_{A1} for $f_{x1} = 930$ Hz, $f_{y1} = 940$ Hz, and $t = 100$ ms.

the minimization of vacant field done by selecting appropriate frequencies.

The second important problem is the nonuniform distribution of points even when the sampling frequency is constant (the time delay between the readings of consecutive point positions is constant and equal to the delay between consecutive OCT measurements). The reason for this problem is the nonequal distribution of speeds on the two axes, corresponding to respective sine waves. This means that if point measurements are carried out at equal time intervals, the center of the test sample will be determined by the smallest number of measurement points. The edges will contain more measurement points that will overlap and the distribution of average intensity in the image will also be uneven.

The goal of the numerical analysis of the scanning beam trajectory for selected frequencies is to study the area coverage by the generated points related to Lissajous curves. The simulation analyzes the coverage by dividing the whole scanning field into sectors of 1 μm^2; a given sector is counted as covered when the x and y coordinates of a generated point belong to that sector. Fig. 5(a) shows the graph of percent coverage of the scanning field S_{A1} for $f_{x1} = 930$ Hz and $f_{y1} = 940$ Hz versus time, with the number of points generated.

In the time of 100 ms, there are 20 000 points generated that cover 94.11% of the entire field S_{A1}. The large number of points or the long time does not guarantee complete coverage of the scanning field. After 100 ms, the coverage value is saturated. Further increase in generated points does not increase the coverage ratio. This happens when the trajectory repeats the loop and does not provide new measurement points. The distribution of points for 100 ms is shown in Fig. 5(b). It is uniform in the central region, with a visible increase in points density close to the edges of the measurement field. This effect is a natural result caused by equal sampling when the speed of sampling is decreasing. To analyze this effect closer, each point of the calculated trajectory was replaced by a 2-D intensity distribution, corresponding to the size of an Airy disk calculated for the experimental system. Here, it is represented by a kernel of 23 × 23 pixels with a Gaussian distribution of values around the central pixel [Fig. 6(a)]. Accordingly, only for the central pixel of the kernel ([x, y] coordinates [12, 12]) does the intensity equal 1. Placing the kernel onto each of the generated points, we can sum up the intensity on the surface over the measurement time and plot the intensity distribution as presented in Fig. 6(b). It is worth noting that the central area is very uniform. Unfortunately, the central area is surrounded by a ring and its area is only approximately 50% of the whole area S_{A1}. There are also four peaks located in the corners. Fig. 7(a) presents the graph of percent coverage of the scanning field S_{A2} for $f_{x2} = 940$ Hz and $f_{y2} = 943$ Hz versus time, with the number of points generated. In the time of 100 ms, 20 000 points were generated, covering 75.88% of field S_{A2}. Due to a different set of frequencies, the trajectory is completely changed. The coverage reaches 94% after 200 ms, twice longer than for the previously presented frequencies (Fig. 5). The distribution of the points in the trajectory is shown in Fig. 7(b). Applying the same method for the calculation of the intensity distribution with a simulated Airy spot, we were able to compare the distributions for different time periods; Fig. 8(a) corresponds to the 100-ms time period, and Fig. 8(b) corresponds to 200 ms. Fig. 8(a) and (b) reveal the complex behavior of this scanning technique. After 100 ms, one diagonal direction is covered; whereas after 200 ms, a second diagonal seems to be covered even with a higher density of points. This scenario proves the essential role of proper selection of frequencies for experimental scanning of objects.

V. Experimental Verification of Lissajous Patterns

The trajectory of Lissajous patterns is measured with the system presented in Fig. 1. Fig. 9(a) shows the distribution of points on the PSD for $f_{x1} = 930$ Hz, $f_{y1} = 940$ Hz, and $t = 100$ ms. Next, the coordinates of points are recalculated according to the scanned area on sample S_{A1}. The intensity distribution is calculated by placing the simulated Airy spot on each point captured in the experiment. The result obtained in this case [Fig. 9(b)] can be compared with the result of the simulation shown in Fig. 6(b). The intensity distribution on both graphs is very similar. The main difference is the visible skew of experimental data due to scanner work. This effect slightly changes the distribution of the points on the scanned area, but it has a small effect on the intensity distribution and resulting OCT imaging process.

The experimental data for $f_{x2} = 940$ Hz, $f_{y2} = 943$ Hz, and $t = 200$ ms were processed similarly, and the results are shown in Fig. 10. When comparing the intensity distributions [Figs. 8(b) and 10(b)], one may notice comparable features of distributions with two biggest peaks and two smaller peaks on the corners of the scanning area. Both of the experimen-

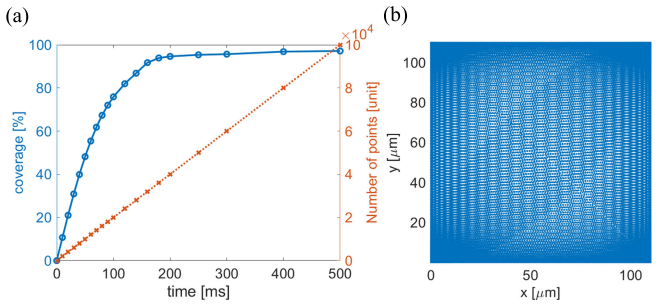

Fig. 7. Numerical data analysis of field S_{A2} for $f_{x2} = 940$ Hz and $f_{y2} = 943$ Hz. (a) Graph of percent coverage of the measurement field versus time. (b) 2-D points distribution after $t = 200$ ms; 40 000 points; and coverage 94.63%.

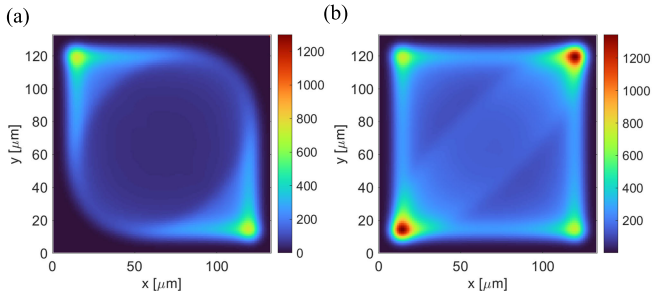

Fig. 8. Numerical data analysis of field S_{A2} for $f_{x2} = 940$ Hz and $f_{y2} = 943$ Hz. (a) 2-D intensity distribution after $t = 100$ ms; 20 000 points; and coverage 75.88%. (b) 2-D intensity distribution after $t = 200$ ms; 40 000 points; and coverage 94.63%.

tal results confidently demonstrate good agreement with the results of the numerical simulations presented in Section IV.

The control of the scanning beam position by the PSD allows to filter out the data points with the same repeating positions. This approach was applied for experimental data processing for display images in Section VI.

VI. Characterization and OCT Imaging With Endomicroscopy Probe

The correct operation of the endomicroscopy probe was verified during OCT scanning and imaging of test samples. The OCT imaging was performed by an endomicroscopy probe working in a transverse scanning mode, which uses a two-axis electrothermal actuator and Lissajous curves. The experiment was carried out for two pairs of scanning frequencies as described above. The first part of the experiment was focused on the determination of the lateral resolution, as well as on the scanning area of the probe. The USAF target 1951 (Thorlabs) was used as a first test sample [Fig. 11(a)]. The second part of the experiment was focused on 2-D and 3-D OCT imaging of layered test samples. The second test sample was fabricated as a thin pattern of polymer material (Microposit[1] S1813[1] photoresist, Shipley, Marlborough, MA, USA) with thickness $d_p = 20$ μm and refractive index $n_p = 1.59$ ($\lambda = 1060$ nm), deposited on a glass substrate with a refractive index $n_s = 1.46$ (Borofloat[1]33, Schott, Jena, Germany) [Fig. 11(b)].

As a third test sample, a phantom with light-scattering properties in the form of a scotch tape (50 μm thickness) on a glass substrate was used.

[1]Registered trademark.

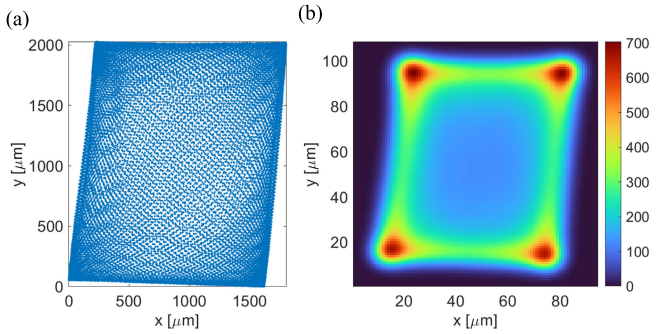

Fig. 9. Experimental data analysis for S_{A1}, $f_{x1} = 930$ Hz, $f_{y1} = 940$ Hz, $t = 100$ ms, and 20 000 points. (a) 2-D distribution of points on the PSD. (b) Intensity distribution for the sample.

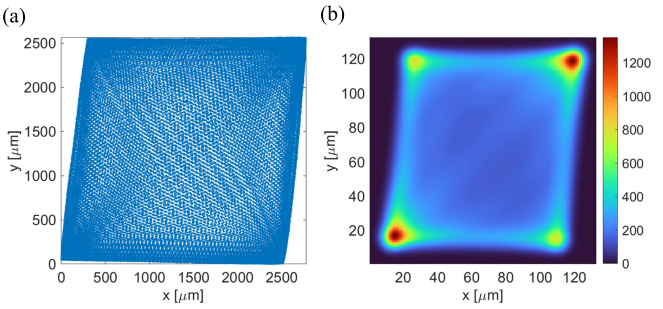

Fig. 10. Experimental data analysis for S_{A2}, $f_{x2} = 940$ Hz, $f_{y2} = 943$ Hz, $t = 200$ ms, and 20 000 points. (a) 2-D distribution of points on the PSD. (b) Intensity distribution for the sample.

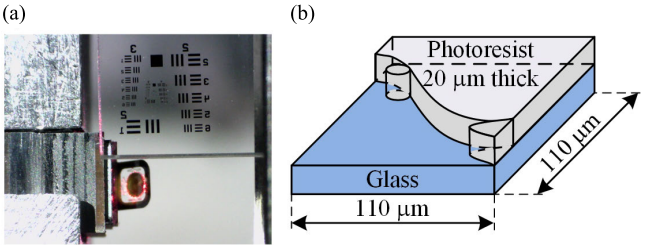

Fig. 11. Test samples: (a) USAF 1951 target and (b) photoresist deposited on a glass.

The analysis was carried out with the following parameters: $t_1 = 100$ ms, for $f_{x1} = 930$ Hz and $f_{y1} = 940$ Hz; and $t_2 = 200$ ms, for $f_{x2} = 940$ Hz and $f_{y2} = 943$ Hz. The results of the numerical analysis presented above, such as coverage of measurement field versus time, and pixel size were applied in the analysis of the experimental data to obtain proper OCT images.

Figs. 12–17 show the results of OCT measurements of group 5, elements 1–3 of the USAF test target, with the corresponding widths of these patterns: element 1, $W_{5\_1} = 15.63$ μm; element 2, $W_{5\_2} = 13.92$ μm; and element 3, $W_{5\_3} = 12.40$ μm. The signal measured by the endomicroscopic probe and the position of the scanning beam measured by the PSD is shown in Figs. 12(a), 13(a), 14(a), 15(a), 16(a), and 17(a). The insets in Figs. 12(a), 13(a), 14(a), 15(a), 16(a), and 17(a) show the distribution of light intensity (Airy disk) in the focal plane. The green dashed line shows the area for which the cross section of the light intensity distributions has been determined according to the x-axis. The cross section of light intensity along the x-axis presented in Figs. 12(c), 13(c), 14(c), 15(c), 16(c), and 17(c) was calculated

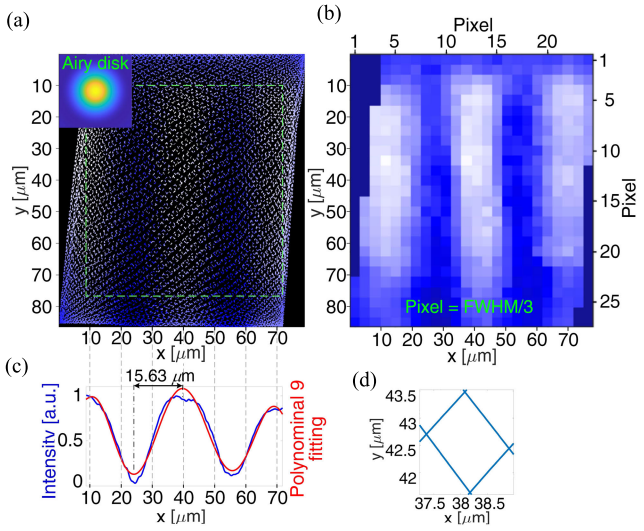

Fig. 12. OCT imaging of the USAF target at 15.63 μm and f_{x1} = 930 Hz and f_{y1} = 940 Hz: (a) 2-D points intensity and distribution; (b) 2-D OCT images presented in pixels scale; (c) cross section of the 2-D light intensity; and (d) Lissajous trajectory in the center of the 2-D image.

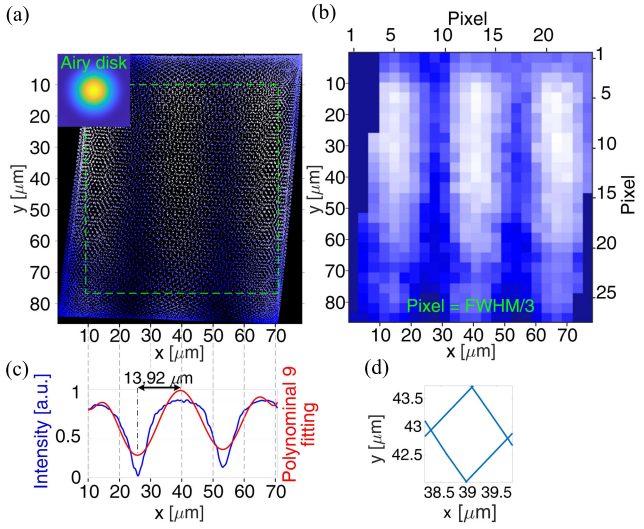

Fig. 13. OCT imaging of the USAF target at 13.92 μm and f_{x1} = 930 Hz and f_{y1} = 940 Hz: (a) 2-D points intensity and distribution; (b) 2-D OCT images presented in pixels scale; (c) cross section of the 2-D light intensity; and (d) Lissajous trajectory in the center of the 2-D image.

not for a single cross-sectional line (single y-value) because measurement points are unevenly distributed on the scanned area (including x-axis) caused by the Lissajous trajectory scanning. In addition for a single cross-sectional line, we have a relatively small number of measurement points. In such a case, the min–max position would be difficult to determine correctly. In the presented analyses for each case of scan, the subsequent cross sections were extracted for all possible y-axis values in the area marked by a green dashed line. The subsequent cross sections were superimposed on each other to obtain the final cross section of light intensity presented, respectively, in Figs. 12(c), 13(c), 14(c), 15(c), 16(c), and 17(c). Thanks to this operation, we have a high density of measurement points of light intensity as a function of position

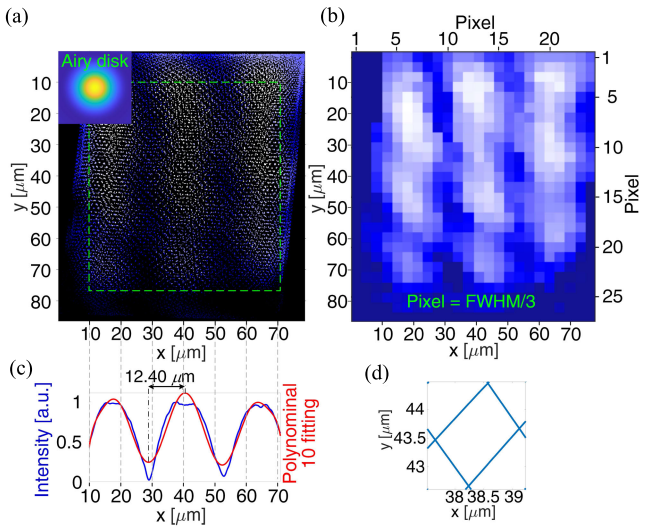

Fig. 14. OCT imaging of the USAF target at 12.40 μm and f_{x1} = 930 Hz and f_{y1} = 940 Hz: (a) 2-D points intensity and distribution; (b) 2-D OCT images presented in pixels scale; (c) cross section of the 2-D light intensity; and (d) Lissajous trajectory in the center of the 2-D image.

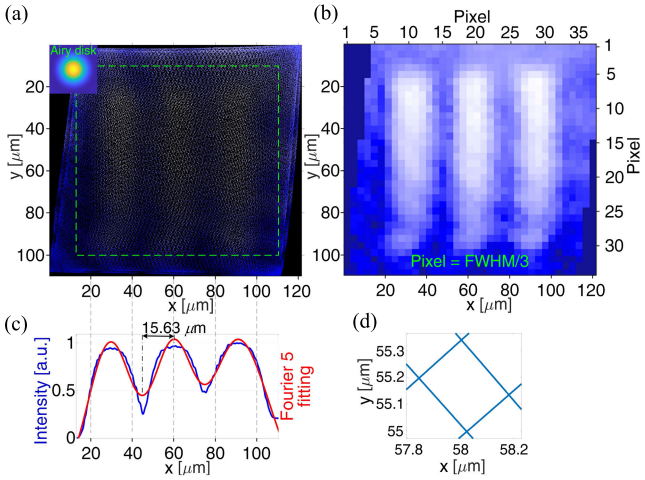

Fig. 15. OCT imaging of the USAF target at 15.63 μm and f_{x2} = 940 Hz and f_{y2} = 943 Hz: (a) 2-D points intensity and distribution; (b) 2-D OCT images presented in pixels scale; (c) cross section of the 2-D light intensity; and (d) Lissajous trajectory in the center of the 2-D image.

on the x-axis. (It should be noted that we do not add values from following subsequent cross sections together because the density of points is different and this would lead to incorrect results.) After superimposed subsequent cross sections, the background of the signal was subtracted to highlight the min–max position. Next, the function fitting was applied to determine the min/max position. This approach provides precise determination of the min–max position, which was used to determine the scanning ranges of the endomicroscopic probe. The corresponding OCT en-face projections obtained by the probe are presented in Figs. 12(b), 13(b), 14(b), 15(b), 16(b), and 17(b). Figs. 12(d), 13(d), 14(d), 15(d), 16(d), and 17(d) show the Lissajous trajectory in the center of the acquired image, where the trajectory density is lowest. The distance between the trajectories is less than 2 μm for frequencies

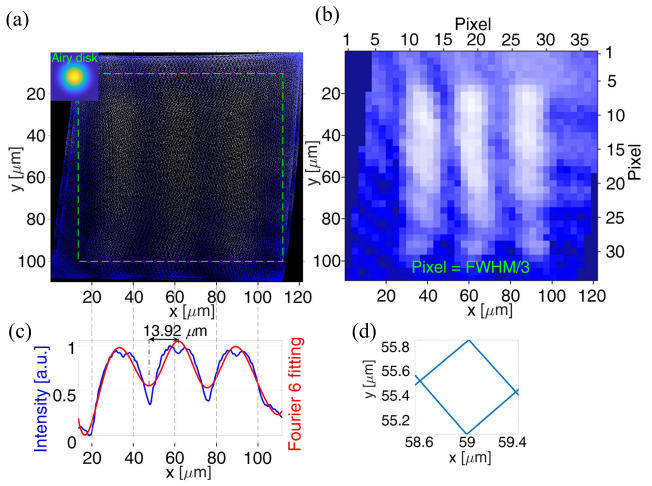

Fig. 16. Data analysis for USAF target at 13.92 μm and $f_{x2} = 940$ Hz and $f_{y2} = 943$ Hz: (a) 2-D points intensity and distribution; (b) 2-D OCT images presented in pixels scale; (c) cross section of the 2-D light intensity; and (d) Lissajous trajectory in the center of the 2-D image.

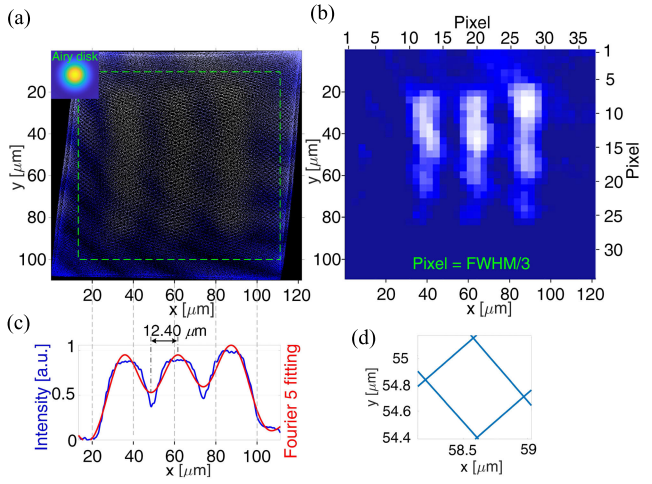

Fig. 17. OCT imaging of the USAF target at 12.40 μm and $f_{x2} = 940$ Hz and $f_{y2} = 943$ Hz: (a) 2-D points intensity and distribution; (b) 2-D OCT images presented in pixels scale; (c) cross section of the 2-D light intensity; and (d) Lissajous trajectory in the center of the 2-D image.

$f_{x1} = 930$ Hz and $f_{y1} = 940$ Hz, and less than 0.8 μm for frequencies $f_{x2} = 940$ Hz and $f_{y2} = 943$ Hz; thus, both distances are much smaller than the pixel size.

The 2-D-OCT images obtained by the probe correctly reproduced the shape of the USAF target elements with widths of 15.63 and 13.92 μm (Figs. 12 and 13, as well as Figs. 15 and 16). Analysis of the images showed that the lateral resolution of the endomicroscopy probe is at the level of $L_r = 13.92$ μm, which corresponds to the width of the pattern of element 2, group 5 in the USAF target. For smaller patterns of the USAF target (element 3, group 5) with width $W_{5\_3} = 12.40$ μm, the shape of the imaged patterns is distorted and the contrast is low [Figs. 14(a) and (c) and 17(a) and (c)]. The size of the scanning areas S_{A1} and S_{A2} for the probe was determined using the USAF target; however, analysis was carried out for patterns with widths of 15.63 and 13.92 μm for which the resolution of the endomicroscopic probe is sufficient. The cross sections of signal intensities on the x-axis for individual images made for the USAF target are presented in Figs. 12(c), 13(c), 15(c), and 16(c). Figs. 12(c), 13(c), 15(c), and 16(c) show the minimum and maximum of the signal for the analyzed image, and knowing the width of the patterns, it was possible to determine the scanning range on the x-axis and then on the y-axis. In addition, analysis of images shows that the difference between the scan ranges on the x- and y-axes for the chosen frequencies is relatively small, especially for the second pair of frequencies. Measured scanning areas are presented in Table I. The analysis of Figs. 12(b), 13(b), 15(b), and 16(b) allows the determination of contrast-to-noise ratio (CNR) defined as a difference in signal intensities between the selected area of the picture—USAF target mirror part and USAF target glass part, divided by the standard deviation of the pure image noise, the CNR = 5.2.

The skew of the OCT images results from a slight tilt of the scanning mirror on the y-axis in the He–Ne laser -> scanning mirror -> PSD circuit from the ideal position of 45° (relative to the laser or PSD direction). The value of additional mirror deflection is $\alpha_{add} = 2.92°$. When the mirror is tilted by an angle α, the angle of the light beam reflected from it will be changed as $2{*}\alpha_{add}$ (doubles of angle). This is visible as the skew of the OCT images by an angle $\alpha_{oct} = 2 \times 2.92° = 5.84°$. The skew of the OCT images does not significantly impact the shape of the mapped objects, and visible OCT images for USAF target are not distorted. The skew of the OCT images was taken into account during analyzing the scanning area. The value of the scanning area for a skew image was determined and converted using $\cos(\alpha_{img})$ to the value of the scanning field for a straight OCT image. The difference between those two values was taken as the accuracy of scanning area Table I. The impact of additional mirror tilt on the scanning area is small below 0.57 μm for all ranges.

In order to compare the impact of using both pairs of frequencies on the size of the scanned area, measurements were carried out using the sample presented in Fig. 11(b). The scanning field for both pairs of frequencies f_{x1} and f_{y1} is marked by a red line in Figs. 18 and 19. The signal measured by the endomicroscopic probe and the position of the scanning beam measured by the PSD is shown in Figs. 18(a) and 19(a). The corresponding 2-D OCT en-face projections obtained by the probe are presented in Figs. 18(b) and 19(b). The dark blue color represents the glass area, and the lighter white-blue colors represent an area with the shape of deposited S1813 photoresist. The corresponding 3-D OCT layered projections obtained by the probe are presented in Figs. 18(c) and 19(c). The shape of the S1813 photoresist is represented as a top layer, and glass is represented as a bottom layer.

The phantom based on scotch tape on a glass substrate thanks to scattering properties is often used to confirm proper operations of OCT imaging systems. The scotch tape-based sample was scanned by the probe with operational frequency $f_{x2} = 940$ Hz and $f_{y2} = 943$ Hz to ensure maximum scanning area. The OCT image in the form of a b-scan for the glass substrate is shown in Fig. 20(a). The glass surface is very clearly visible. Slight changes in signal intensity result from

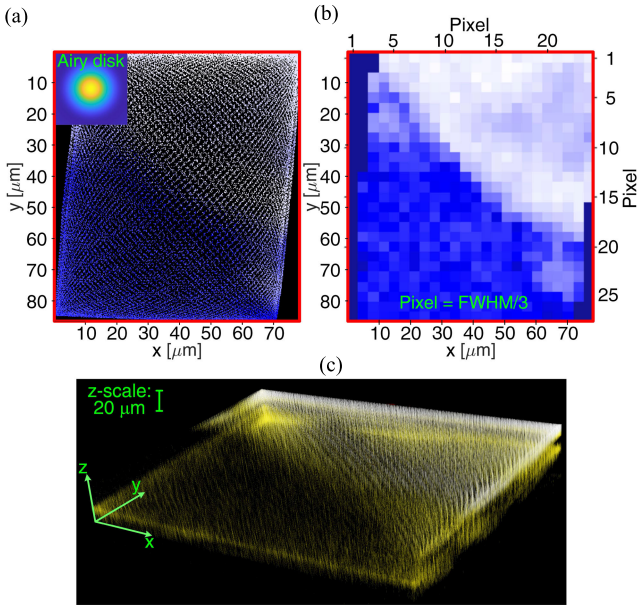

Fig. 18. OCT imaging of test sample for scanning frequency: $f_{x1} = 930$ Hz and $f_{y1} = 940$ Hz: (a) signal intensity and beam position; (b) OCT image, 2-D; and (c) OCT image, 3-D.

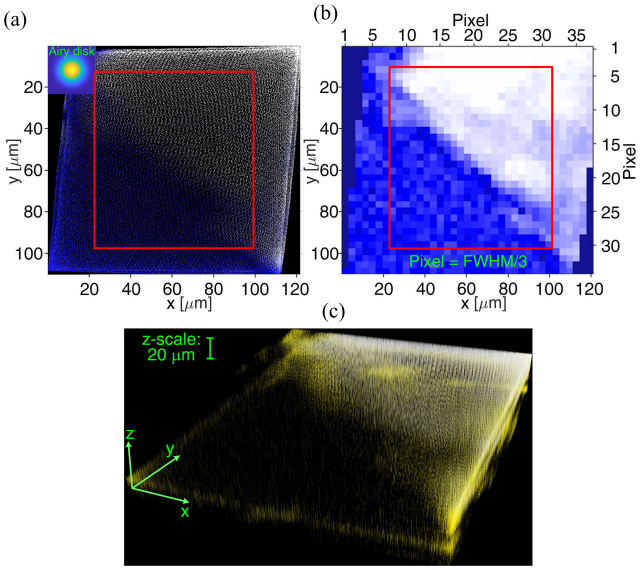

Fig. 19. OCT imaging of a test sample for scanning frequency: $f_{x2} = 940$ Hz and $f_{y2} = 943$ Hz: (a) signal intensity and beam position; (b) OCT image, 2-D; and (c) OCT image, 3-D.

scanning the sample through the moving micromirror. The OCT image in the form of a b-scan of the scotch tape on glass is presented in Fig. 20(b). In the b-scan image, the surface of the scotch tape and the surface of the glass are recognizable. On the scotch tape surface, its heterogeneity is visible in places of higher signal intensity.

As mentioned earlier, it is important to choose the right voltage and frequency on the x- and y-axes to generate the right Lissajous scanning trajectory. Our measurements showed that both pairs of frequencies $f_{x1} = 930$ Hz and $f_{y1} = 940$ Hz, and $f_{x2} = 940$ Hz and $f_{y2} = 943$ Hz and allow for the correct OCT imaging of the test structures. The OCT imaging quality of the endomicroscopic probe for both frequency pairs and

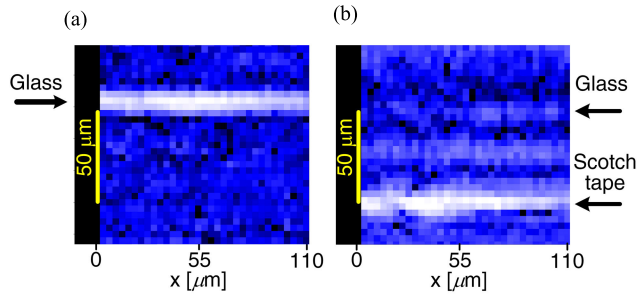

Fig. 20. OCT imaging b-scan: (a) glass and (b) scotch tape on glass.

for the test structures used is similar. It is worth mentioning that for the first pair of scanning frequencies, i.e., $f_{x1} = 930$ Hz and $f_{y1} = 940$ Hz, the obtained scanning range on the x- and y-axes is not the same $S_{A1} = 71.47 \times 86.48$ μm; the difference being 15.01 μm. In the case of a second frequency pair of $f_{x2} = 940$ Hz and $f_{y2} = 943$ Hz, the resulting scan range is almost identical on both the x- and y-axes $S_{A2} = 110.58 \times 110.05$ μm, and the difference between the axes is only 0.53 μm. The S_{A2} scanning area is the maximum achievable for the probe which uses a two-axis electrothermal scanner. Increasing the frequency or voltage to increase the scanning range is not recommended. Using a higher supply voltage than $U_{dc} = 2$ V and $U_{ac} = 0.06$ V may damage the actuator. Additionally increasing the operating frequency above the $f_{x2} = 940$ Hz, $f_{y2} = 943$ Hz will cause the actuator to work in resonance and mechanical coupling between the x- and y-axes. In this case, the Lissajous trajectories will be unstable and impossible to control. In summary, the preferred scanning frequency for the probe is: f_{x2} and f_{y2} in comparison with f_{x1} and f_{y1}. For f_{x2} and f_{y2} frequencies, we obtain the largest scanning area and practically the same scanning range on both the x- and y-axes and a higher density of Lissajous trajectory. These parameters are important for proper OCT imaging by endomicroscopic applications. However, scanning with using f_{x2} and f_{y2} frequencies takes a little bit more time $t_{s2} = 0.2$ s corresponds to 5 frames per second (fps) in comparison to the f_{x1} and f_{y1} frequencies scanning takes $t_{s1} = 0.1$ s corresponds to 10 fps. However, a slightly longer scanning time will not significantly affect the scanning itself because we assume that the scanned structures will be stationary.

VII. Conclusion

This article describes an innovative endomicroscopy probe fabricated with MOEMS/MEMS technology, intended for imaging examined structures using OCT techniques, and scanning with the use of Lissajous trajectories. The test results demonstrate the correct operation of the endomicroscopic probe, which allows scanning of structures over a relatively large scanning area equal to 71.47×86.48 μm with a frame rate of 10 fps or a maximum scanning area equal to 110.58×110.05 μm with the frame rate of 5 fps depending on the driving signal (voltage and frequencies) delivered to electrothermal actuator. The endomicroscopic probe is capable of scanning samples with a high transverse resolution at the level of 14 μm and an axial resolution of 4.96 μm. The

connection of the MOEMS Mirau microinterferometer with a MEMS two-axis electrothermal actuator and analyzing the scanning trajectory with Lissajous curves allow for effective and fast 2-D and 3-D imaging of the examined structures by OCT techniques. In the future, the presented MOEMS probe with its operating parameters (axial and lateral resolution, scanning area, scanning speed, and contrast to noise) is an attractive solution for potential applications in medical endomicroscopic devices for 2-D and 3-D imaging using OCT method.

ACKNOWLEDGMENT

Przemysław Struk is with the Department of Optoelectronics, Faculty of Electrical Engineering, Silesian University of Technology, 44-100 Gliwice, Poland (e-mail: Przemyslaw.Struk@polsl.pl).

Sylwester Bargiel is with the FEMTO-ST Institute, 25030 Besançon cedex, France (e-mail: sylwester.bargiel@femto-st.fr).

Michal Józwik and Bartosz Mirecki are with the Faculty of Mechatronics, Institute of Micromechanics and Photonics, Warsaw University of Technology, 02-525 Warsaw, Poland (e-mail: michal.jozwik@pw.edu.pl; bartosz.mirecki.stud@pw.edu.pl).

Maciej Wojtkowski and Christophe Gorecki are with the ICTER - International Centre for Translational Eye Research, 01-230 Warsaw, Poland, and also with the ICHF - Institute of Physical Chemistry Polish Academy of Sciences, 01-224 Warsaw, Poland (e-mail: mwojtkowski@ichf.edu.pl; cgorecki@ichf.edu.pl).

Huikai Xie was with the Department of Electrical and Computer Engineering, University of Florida, Gainesville, FL 32611 USA. He is now with Beijing Institute of Technology, Beijing 100081, China (e-mail: hk.xie@ieee.org).

REFERENCES

[1] A. Wartak et al., "In vivo optical endomicroscopy: Two decades of translational research towards next generation diagnosis of eosinophilic esophagitis," *Transl. Med. Commun.*, vol. 6, no. 1, pp. 1–19, Jan. 2021, doi: 10.1186/s41231-020-00080-z.

[2] L. van Manen et al., "The clinical usefulness of optical coherence tomography during cancer interventions," *J. Cancer Res. Clin. Oncol.*, vol. 144, no. 10, pp. 1967–1990, Oct. 2018, doi: 10.1007/s00432-018-2690-9.

[3] R. C. Fitzgerald, A. C. Antoniou, L. Fruk, and N. Rosenfeld, "The future of early cancer detection," *Nature Med.*, vol. 28, no. 4, pp. 666–677, Apr. 2022, doi: 10.1038/s41591-022-01746-x.

[4] P. A. Testoni and B. Mangiavillano, "Optical coherence tomography in detection of dysplasia and cancer of the gastrointestinal tract and bilio-pancreatic ductal system," *World J. Gastroenterol.*, vol. 14, no. 42, p. 6444, Nov. 2008, doi: 10.3748/wjg.14.6444.

[5] C. Ren et al., "Multi-center clinical study using optical coherence tomography for evaluation of cervical lesions *in-vivo*," *Sci. Rep.*, vol. 11, no. 1, pp. 1–9, Apr. 2021, doi: 10.1038/s41598-021-86711-3.

[6] J. G. Fujimoto, C. Pitris, S. A. Boppart, and M. E. Brezinski, "Optical coherence tomography: An emerging technology for biomedical imaging and optical biopsy," *Neoplasia*, vol. 2, nos. 1–2, pp. 9–25, Jan. 2000, doi: 10.1038/sj.neo.7900071.

[7] J. Wang, Y. Xu, and S. A. Boppart, "Review of optical coherence tomography in oncology," *J. Biomed. Opt.*, vol. 22, no. 12, Dec. 2017, Art. no. 121711, doi: 10.1117/1.jbo.22.12.121711.

[8] J. Li et al., "Ultrathin monolithic 3D printed optical coherence tomography endoscopy for preclinical and clinical use," *Light, Sci. Appl.*, vol. 9, no. 1, p. 124, Jul. 2020, doi: 10.1038/s41377-020-00365-w.

[9] J. G. Fujimoto, "Optical coherence tomography for ultrahigh resolution in vivo imaging," *Nature Biotechnol.*, vol. 21, no. 11, pp. 1361–1367, Nov. 2003, doi: 10.1038/nbt892.

[10] B. E. Bouma et al., "Optical coherence tomography," *Nature Rev. Methods Primers*, vol. 2, no. 1, pp. 1–79, Oct. 2022, doi: 10.1038/s43586-022-00162-2.

[11] D. S. Schoeb et al., "Ex-vivo evaluation of miniaturized probes for endoscopic optical coherence tomography in urothelial cancer diagnostics," *Ann. Med. Surg.*, vol. 77, May 2022, Art. no. 103597, doi: 10.1016/j.amsu.2022.103597.

[12] G. J. Tearney et al., "In vivo endoscopic optical biopsy with optical coherence tomography," *Science*, vol. 276, no. 5321, pp. 2037–2039, Jun. 1997, doi: 10.1126/science.276.5321.2037.

[13] M. J. Gora, M. J. Suter, G. J. Tearney, and X. Li, "Endoscopic optical coherence tomography: Technologies and clinical applications [Invited]," *Biomed. Opt. Exp.*, vol. 8, no. 5, p. 2405, May 2017, doi: 10.1364/boe.8.002405.

[14] W. Jung, D. T. McCormick, J. Zhang, L. Wang, N. C. Tien, and Z. Chen, "Three-dimensional endoscopic optical coherence tomography by use of a two-axis microelectromechanical scanning mirror," *Appl. Phys. Lett.*, vol. 88, no. 16, Apr. 2006, Art. no. 163901, doi: 10.1063/1.2195092.

[15] T. Wu et al., "Side-viewing endoscopic imaging probe for swept source optical coherence tomography," *Opt. Commun.*, vol. 467, Jul. 2020, Art. no. 125596, doi: 10.1016/j.optcom.2020.125596.

[16] J. Sun et al., "3D In vivo optical coherence tomography based on a low-voltage, large-scan-range 2D MEMS mirror," *Opt. Exp.*, vol. 18, no. 12, p. 12065, May 2010, doi: 10.1364/oe.18.012065.

[17] P. Struk et al., "Swept source optical coherence tomography endomicroscope based on vertically integrated mirau micro interferometer: Concept and technology," *IEEE Sensors J.*, vol. 15, no. 12, pp. 7061–7070, Dec. 2015, doi: 10.1109/JSEN.2015.2469547.

[18] K. Hwang, Y.-H. Seo, and K.-H. Jeong, "Microscanners for optical endomicroscopic applications," *Micro Nano Syst. Lett.*, vol. 5, no. 1, pp. 1–11, Dec. 2017, doi: 10.1186/s40486-016-0036-4.

[19] T. Liu, T. Pan, P. Wang, S. Qin, and H. Xie, "Scanning optimization of an electrothermally-actuated MEMS mirror for applications in optical coherence tomography endoscopy," *Sens. Actuators A, Phys.*, vol. 335, Mar. 2022, Art. no. 113377, doi: 10.1016/j.sna.2022.113377.

[20] M. Strathman et al., "MEMS scanning micromirror for optical coherence tomography," *Biomed. Opt. Exp.*, vol. 6, no. 1, p. 211, Jan. 2015, doi: 10.1364/boe.6.000211.

[21] Y. Tang, J. Li, L. Xu, J.-B. Lee, and H. Xie, "Review of electrothermal micromirrors," *Micromachines*, vol. 13, no. 3, p. 429, Mar. 2022, doi: 10.3390/mi13030429.

[22] C. Gorecki and S. Bargiel, "MEMS scanning mirrors for optical coherence tomography," *Photonics*, vol. 8, no. 1, p. 6, Dec. 2020, doi: 10.3390/photonics8010006.

[23] B. R. Samanta, F. Pardo, T. Salamon, R. Kopf, and M. S. Eggleston, "Low-cost electrothermally actuated MEMS mirrors for high-speed linear raster scanning," *Optica*, vol. 9, no. 2, p. 251, Feb. 2022, doi: 10.1364/optica.446407.

[24] Y.-H. Seo, K. Hwang, and K.-H. Jeong, "Compact OCT endomicroscopic catheter using flip-chip bonded Lissajous scanned electrothermal MEMS fiber scanner," in *Proc. IEEE 30th Int. Conf. Micro Electro Mech. Syst. (MEMS)*, Las Vegas, NV, USA, Jan. 2017, pp. 518–521, doi: 10.1109/MEMSYS.2017.7863457.

[25] J. Wang, G. Zhang, and Z. You, "Design rules for dense and rapid Lissajous scanning," *Microsystems Nanoengineering*, vol. 6, no. 1, pp. 1–7, Nov. 2020, doi: 10.1038/s41378-020-00211-4.

[26] W. Du, G. Zhang, and L. Ye, "Image quality analysis and optical performance requirement for micromirror-based Lissajous scanning displays," *Sensors*, vol. 16, no. 5, p. 675, May 2016, doi: 10.3390/s16050675.

[27] Q. A. A. Tanguy et al., "Real-time Lissajous imaging with a low-voltage 2-axis MEMS scanner based on electrothermal actuation," *Opt. Exp.*, vol. 28, no. 6, p. 8512, Mar. 2020, doi: 10.1364/oe.380690.

[28] P. Struk et al., "Swept-source optical coherence tomography microsystem with an integrated mirau interferometer and electrothermal micro-scanner," *Opt. Lett.*, vol. 43, no. 19, p. 4847, Oct. 2018, doi: 10.1364/ol.43.004847.

[29] A. F. Fercher, W. Drexler, C. K. Hitzenberger, and T. Lasser, "Optical coherence tomography–principles and applications," *Rep. Prog. Phys.*, vol. 66, no. 2, pp. 239–303, Feb. 2003, doi: 10.1088/0034-4885/66/2/204.

[30] W. Drexler and J. G. Fujimoto, "Introduction to optical coherence tomography," in *Optical Coherence Tomography Technology and Applications*. New York, NY, USA: Springer, 2008, pp. 1–40.

[31] D. Durini, *High Performance Silicon Imaging Fundamentals and Applications of CMOS and CCD Sensors* (A volume in Woodhead Publishing Series in Electronic and Optical Materials), 2nd ed. Amsterdam, The Netherlands: Science Direct, 2020.

[32] G. Dougherty, *Digital Image Processing for Medical Applications*. Cambridge, U.K.: Cambridge Univ. Press, 2009.

[33] U. J. Brik, *Super-Resolution Microscopy: A Practical Guide*. Hoboken, NJ, USA: Wiley, 2017.

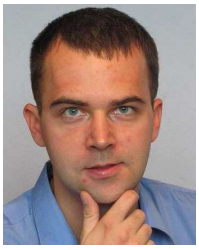

Przemysław Struk received the M.Sc. degree in electronics and telecommunications engineering and the Ph.D. degree in electronics from the Faculty of Mathematics and Physics and the Faculty of Electrical Engineering, Silesian University of Technology, Gliwice, Poland, in 2007 and 2013, respectively.

He was a Postdoctoral Research Fellow with the Institute of FEMTO-ST/University of Franche-Comté, Besançon, France, from 2013 to 2015. He is currently a Professor with the Department of Optoelectronics, Silesian University of Technology. His scientific interest is focused on the development of the optical coherence tomography technique, the development of modern MEMS/micro-opto-electromechanical systems (MOEMS) devices for biomedical applications, and the design and fabrication of photonics circuits and sensor structures.

Sylwester Bargiel received the Ph.D. degree from the Faculty of Microsystem Electronics and Photonics, Wroclaw University of Science and Technology, Wrocław, Poland, in 2005.

He joined the Department of Micro Nano Sciences and Systems (MN2S), FEMTO-ST Institute (CNRS UMR 6174), Besançon, France, as the Marie-Curie Fellow Researcher, in 2007. His scientific activity is focused on the development of fully integrated micro-opto-electromechanical systems (MOEMS)-based optical instruments: miniature optical coherency tomography (OCT) and confocal microscopy on-chip for biomedical applications.

Michal Józwik received the M.Sc. degree in automatics and robotics from the Warsaw University of Technology, Warsaw, Poland, in 1999, the Ph.D. degree in optical engineering from the Warsaw University of Technology and University of Franche-Comté, Besançon, France, in 2004.

From 2004 to 2006, he was a Postdoctoral Researcher with the Institute of FEMTO-ST, Besançon, France. He is a Researcher and a Lecturer with Warsaw University of Technology, Warsaw, Poland, where he became an Associate Professor in 2017 and has been the Head of the Photonic Engineering Division since 2019. His scientific interest is focused on optical metrology—full-field methods and instruments (interferometry and digital holography) applied for technology, experimental mechanics and material science, optical and numerical methods of image processing, integrated optics, and MEMS/micro-opto-electromechanical systems (MOEMS)—technology, fabrication, characterization, and applications.

Bartosz Mirecki received the M.Sc. degree in photonics engineering from Warsaw University of Technology, Warsaw, Poland, in 2021, where he is pursuing the Ph.D. degree with the Faculty of Mechatronics, focusing on the laboratory setup and advanced fringe pattern analysis in lens-less holographic microscopy.

Maciej Wojtkowski received the Ph.D. degree in experimental physics from Nicolaus Copernicus University, Toruń, Poland, in 2003.

He worked as a Postdoctoral Fellow on a joint project between Massachusetts Institute of Technology, Cambridge, MA, USA, and the New England Eye Center, Boston, MA, for two years. Prof. Wojtkowski is currently the Head of the Department of Physical Chemistry of Biological Systems, Institute of Physical Chemistry of the Polish Academy of Sciences, Warsaw, Poland, where he also leads his own research team (Physical Optics and Biophotonics Group) and became the Head of the New Center of Excellence of the International Center for Translational Eye Research (ICTER). His research interests include optical coherence tomography, low-coherence interferometry, and two-photon fluorescence imaging applied to biomedical imaging.

Huikai Xie (Fellow, IEEE) received the B.S. degree in microelectronics from Beijing Institute of Technology, Beijing, China, in 1989, the M.S. degree in photonics from Tufts University, Medford, MA, USA, in 1992, and the Ph.D. degree in electrical and computer engineering from Carnegie Mellon University, Pittsburgh, PA, USA, in 2002.

He worked as an Assistant Professor from 2002 to 2007, an Associate Professor with tenure from 2007 to 2011, and a Full Professor from 2011 to 2020 with the University of Florida, Gainesville, FL, USA. He is currently a Professor with the School of Information and Electronics, Beijing Institute of Technology. He has authored over 360 technical articles and 11 book chapters, and holds over 30 U.S. patents. His current research interests include MEMS/nanoelectromechanical systems (NEMS), optical beam steering, optical communications, near infrared response (NIR) spectroscopy, LiDAR, and optical microendoscopy.

Dr. Xie is a Fellow of SPIE. He is also an Associate Editor of *Sensors and Actuators A: Physical* and IEEE SENSORS LETTERS.

Christophe Gorecki received the Ph.D. degree in optics from the University of Franche-Comté, Besançon, France, in 1983.

He joined the Laboratoire d'Optique P.M. Duffieux (LOPMD), Besançon, as a CNRS Scientist, in 1984. He worked with the University of Tokyo, Tokyo, Japan, where he was engaged in research and development of micro-opto-electromechanical systems (MOEMS) devices, from 1995 to 1998. He was the Director of Research with CNRS, Paris, France, and also the Head of the MOEMS Group, FEMTO-ST Institute, University of Franche-Comté (CNRS UMR 6174), Besançon. He is a Professor with the International Center for Translational Eye Research, Institute of Physical Chemistry, Warsaw, Poland. He has authored or coauthored 237 scientific publications and three book chapters. His scientific interest is focused on the research of MOEMS architectures for micro- and nanosensors as well as the development of metrology methods for the characterization of MEMS/MOEMS devices.

Prof. Gorecki belongs to the Officers and Board of Directors of the SPIE Organization. From 1992 to 1995, he served as the National Secretary for the French Society of Optics (SFO).